Cellulose (2017) 24:1017–1029
DOI 10.1007/s10570-016-1154-0

ORIGINAL PAPER

# $Cu_2O$ nanoparticle-functionalized cellulose-based aerogel as high-performance visible-light photocatalyst

**Xiuping Su · Qian Liao · Lin Liu · Ranju Meng · Zhouqi Qian · Huiying Gao · Juming Yao**

Received: 19 April 2016 / Accepted: 5 December 2016 / Published online: 30 December 2016


**Abstract** $Cu_2O$ nanoparticle (NP)-functionalized cellulose-based aerogel ($Cu_2O$/CBA) with three-dimensional (3D) macroporous structure and abundant active sites was successfully prepared for visible-light photocatalysis via in situ deposition of $Cu_2O$ NPs on cellulose-based aerogel (CBA). Octahedral $Cu_2O$ NPs were formed and anchored onto the surface and inner wall of the cellulose matrix, which acted as a microreactor to prevent aggregation and protect the catalytic character of the $Cu_2O$ NPs. The photocatalytic performance of the $Cu_2O$/CBA composite catalysts was evaluated using degradation of methylene blue (MB) as model pollutant. The effects of catalyst dosage, initial MB concentration, and solution pH on MB photodegradation were investigated. Use of 3D macroporous CBA improved the MB adsorption capacity and extended the absorption of visible-light irradiation. In particular, in situ deposition of $Cu_2O$ in the cellulose matrix enhanced separation of photogenerated electrons and holes via surface-adsorbed molecular oxygen, and consequently the catalytic activity. The photodegradation rate of MB by $Cu_2O$/CBA composite catalyst reached 95.79%, much higher than the value of 73.59% for pure $Cu_2O$. The photodegradation process on the $Cu_2O$/CBA composite catalysts followed an apparent pseudo-first-order kinetic model. The $Cu_2O$/CBA composite catalyst was easily recycled and reused, with 80% MB degradation rate retained even after six cycles of irradiation for 30 min each. Such $Cu_2O$/CBA composite catalysts can be applied for wastewater treatment utilizing solar radiation.

**Keywords** Cellulose matrix · Cuprous oxide nanoparticles · In situ · Visible-light catalysis · Wastewater treatment

## Introduction

Functional micro/nanomaterials with unique physical and chemical properties are currently at the forefront of materials research because of their potential applications in various areas, such as energy conversion (Li et al. 2014; Han et al. 2014), heterogeneous catalysis (Sun et al. 2016), fuel cells (Sanad et al. 2015), gas sensors (Majhi et al. 2014), biosensors (Arcot et al. 2015), and biomedicine (Chiappone et al. 2013). In particular, functional 3D catalytic materials

**Electronic supplementary material** The online version of this article (doi:10.1007/s10570-016-1154-0) contains supplementary material, which is available to authorized users.

X. Su · Q. Liao · L. Liu · Z. Qian · J. Yao (✉)
The Key Laboratory of Advanced Textile Materials and Manufacturing Technology of Ministry of Education, College of Materials and Textiles, Zhejiang Sci-Tech University, Hangzhou 310018, China
e-mail: yaoj@zstu.edu.cn

R. Meng · H. Gao
Jiaxing Vocational Technical College, Jiaxing 314036, China

containing nanocatalyst on a high-surface-area support are being widely investigated because of their functionality and the tailorability of both the nanocatalyst and support materials (Zhang et al. 2014b). For catalytic applications, the large surface area and large amount of edge and corner atoms of ultrafine nanocatalysts distinctly improve the catalytic activity. Accordingly, considerable research effort has been invested to design and prepare 3D support materials to prevent nanocatalyst aggregation and thereby improve the catalytic activity.

$Cu_2O$ is a multifunctional semiconductor that has attracted extensive interest because of its widespread use in electronics, optics, sensors, catalysis, and medical applications (Tilley et al. 2014). $Cu_2O$ has a narrow bandgap (2.0–2.2 eV) and suitable conduction band, contributing to its efficient visible-light absorption and potential for photocatalysis under visible light (Cao et al. 2015). Moreover, $Cu_2O$ is naturally abundant, nontoxic, and relatively cheap, making large-scale fabrication of $Cu_2O$ nanocatalyst possible and rendering it competitive with other, ultraviolet (UV)-light-driven nanocatalysts such as ZnO and $TiO_2$. To date, various $Cu_2O$ nanostructures (cubic, octahedral, nanosphere, nanocage, nanowire, nanoflower, and nanorod) have been fabricated, exhibiting excellent photocatalytic properties for degradation of toxic dyes and other pollutants (Hua et al. 2011; Huang et al. 2012). Unfortunately, such $Cu_2O$ nanostructures tend to aggregate owing to their large surface area and high surface energy, reducing their photocatalytic efficiency in practical applications. Attempts to overcome these problems using a polymeric matrix as a support for growth of $Cu_2O$ nanostructures have been reported. Cao et al. (2013) reported $Cu_2O$/crosslinked-chitosan nanocomposites that exhibited high photocatalytic activity for degradation of X-3B dye compared with pure $Cu_2O$. $Cu_2O$/polyaniline nanocomposites were prepared through oxidative polymerization and showed higher photocatalytic activity than pure $Cu_2O$ due to the combination of $Cu_2O$ NPs and polyaniline (Wang et al. 2013). In addition, Tu et al. prepared a portable photocatalyst by synthesizing regenerated cellulose/graphene oxide composite films and studied its photocatalytic performance in degradation of methyl orange (MO) dye under visible-light irradiation (Tu et al. 2014). The focus in these reports was one-dimensional (1D) or two-dimensional (2D) matrixes as supports for $Cu_2O$ nanostructures.

Cellulose is an abundant renewable natural material with good properties, being soft, ecofriendly, machinable, cheap, and remarkably hydrophilic, making it an attractive support for nanoparticles (Xiong et al. 2013; Zhou et al. 2014; Han et al. 2016). In our previous work, cellulose-based hydrogels were synthesized by grafting acrylic acid and acrylamide, exhibiting excellent adsorption capacity for acid blue 93 and methylene blue from single and binary dye solutions due to their ample functional groups and 3D porous structure (Liu et al. 2015). Anchoring of $Cu_2O$ NPs onto such 3D porous cellulose-based materials improved photocatalysis by preventing nanoparticle (NP) aggregation, facilitated catalyst recycling and reuse, and added new functionality to the cellulose matrix, enabling wider and more efficient application in visible-light photocatalysis.

We present herein a facile method to fabricate highly active and durable bifunctional photocatalysts based on $Cu_2O$ NPs supported on 3D cellulose-based aerogel (CBA). Ultrafine $Cu_2O$ NPs were grown in situ on the surface and pore walls of CBA by chemical reduction of $Cu^{2+}$ to $Cu^{+}$ under mild conditions. The target $Cu_2O$ NP-functionalized CBA ($Cu_2O$/CBA) was obtained, exhibiting high surface area and hierarchical porous structure. Furthermore, introduction of carboxyl and amino functional groups into the cellulose matrix strengthened the interaction between the $Cu_2O$ NPs and CBA, improved the adsorption capacity for dyes, and consequently enhanced the catalytic activity and durability of the $Cu_2O$ nanocatalyst. Owing to the unique structural and functional properties of the different components in this catalyst system, and the synergistic effect between them, the as-prepared photocatalyst exhibited remarkably high and stable catalytic activity against cationic dye MB. Degradation of MB was achieved in only 60 min at room temperature even with $Cu_2O$ content as low as 5 wt%. Moreover, the degradation rate remained high at 80% after six successive reaction cycles.

## Experimental

### Materials

Cellulose powder with particle size of 25 μm was purchased as raw material from Aladdin Chemistry

Co. Ltd. Acrylic acid (AA), acrylamide (AM), *N*,*N*′-methylenebisacrylamide (MBA), ammonium persulfate (APS), ethanol, and methylene blue trihydrate (MB) were purchased from Sinopharm Chemical.

## Synthesis of materials

### *Synthesis of CBA*

Cellulose (2 g) was dissolved in 7 wt% NaOH/12 wt% (66 g) urea aqueous solution to obtain cellulose solution according to previous report (Liu et al. 2015). APS (0.2 g) was then added to produce free radicals by stirring for 15 min at room temperature. Afterward, AA (10 g), AM (2 g), and MBA (0.06 g) were successively added to the above solution. The reaction system was transferred into a freezer at −20 °C for 24 h to complete polymerization. The obtained gel was washed with distilled water and ethanol to remove residual monomers and other chemicals. Finally, the washed samples were freeze-dried to obtain CBA.

### *Synthesis of $Cu_2O$-functionalized CBA*

CBA was used as a microreactor for in situ synthesis of $Cu_2O$ NPs. In brief, CBA (0.1 g) was immersed in 100 mL $CuSO_4$ solution (12.5 mmol $L^{-1}$) for 2 h, and the pH of the solution was adjusted to 12. Dilute hydrazine hydrate (v:v = 100:1) was subsequently added to the mixture at room temperature to obtain $Cu_2O$-functionalized CBA with different $Cu_2O$ reduction states controlled by adjusting the reaction time ($t$ = 5, 10, 20, and 60 min). The $Cu_2O$/CBA composite catalysts obtained after different reaction times are denoted as CCs-5, CCs-10, CCs-20, and CCs-60. In another experiment, the prepared CBA was immersed in 100 mL of 12.5, 25, 50, and 100 mmol $L^{-1}$ $CuSO_4$ solutions to obtain $Cu_2O$/CBA composite catalysts with different $Cu_2O$ contents, following a similar fabrication procedure. These $Cu_2O$/CBA composite catalysts obtained using different $CuSO_4$ concentrations are denoted as CCs12.5, CCs25, CCs50, and CCs100. Similarly, octahedral $Cu_2O$ with size of 20 to 200 nm was prepared in absence of CBA as reference sample. Another control sample was prepared by directly blending $Cu_2O$ NPs during CBA formation, denoted as $Cu_2O$-b-CBA.

## Materials characterization

The $Cu_2O$/CBA composite catalysts were ground then subjected to X-ray diffraction (XRD) analysis (D8 Advance, Bruker, USA) with Cu $K_\alpha$ radiation ($\lambda$ = 0.15405 nm) at scan rate of 2° $min^{-1}$ at 40 kV and 40 mA. The chemical structure of each sample was characterized by Fourier-transform infrared (FTIR) spectroscopy (Nicolet 5700, Thermo Electron Corp., USA) using a flat-plate attenuated total reflectance accessory in the range of 400–4000 $cm^{-1}$. Each spectrum was collected at resolution of 2 $cm^{-1}$ with 64 scans. The morphology and elemental composition of the products were investigated by field-emission scanning electron microscopy (FESEM; Ultra 55, Germany) with energy-dispersive X-ray spectroscopy (EDS); the size of the $Cu_2O$ NPs was calculated using ImageJ 1.4 software by measuring at least 50 particles. X-ray photoelectron spectroscopy (XPS) data were obtained using a K-Alpha electron spectrometer (Thermo Fisher Scientific, USA). Thermal stability was determined by thermogravimetric analyzer (TG; Pyris 1, PerkinElmer, USA) at heating rate of 10 °C $min^{-1}$ in $N_2$ environment. Optical diffuse reflectance spectra were measured using an ultraviolet–visible–near infrared (UV–Vis–NIR) spectrometer equipped with an integrating sphere (Lambda 750s, PerkinElmer, USA). $BaSO_4$ was used as reference material, and the polycrystalline samples were ground well before measurement. Photoluminescence (PL) spectra were measured at room temperature using a fluorescence spectrophotometer (F-4600, Hitachi, Japan) with 370-nm excitation source. The $Cu_2O$ content was quantified by atomic absorption spectrometry (AAS; Sollar M6, Thermo, USA) using an air–acetylene flame. Separate hollow cathode lamps radiating at wavelength of 224.8 nm (Cu) were used to determine the amount of Cu.

## Photocatalytic activity

The photocatalytic activity of the as-prepared samples was evaluated in photodegradation of cationic dye MB under visible-light irradiation. Typically, sample was added to 50 mL MB solution at desired concentration and stored in the dark under magnetic stirring for 120 min to reach absorption–desorption equilibrium. Subsequently, photocatalytic reaction was performed

by exposing the solution to irradiation from a 350-W xenon lamp coupled with a UV cutoff filter ($\lambda > 400$ nm). The change in the MB concentration was monitored by recording the UV–Vis absorption at 664 nm at given time intervals.

To optimize the conditions, we systematically investigated the effects of photocatalyst amount (0.3–1.0 g $L^{-1}$), initial dye concentration (25–100 mg $L^{-1}$), and pH (3.0–9.0) on the degradation rate of MB, calculated as

$$D\,(\%) = \frac{c_0 - c_t}{c_0} \times 100\,\%, \quad (1)$$

where $D$ (%) is the degradation of MB at time $t$ in minutes, $c_0$ is the initial MB concentration (mg $L^{-1}$), and $c_t$ is the MB concentration in solution at time $t$ in minutes (mg $L^{-1}$).

## Results and discussion

### Synthesis and characterization of $Cu_2O$/CBA composite catalysts

Scheme 1a illustrates the synthesis strategy applied for the $Cu_2O$/CBA composite catalysts. First, CBA with 3D porous structure and various functional groups ($-COO^-$, $-NH_2$, –OH) was synthesized by grafting AA and AM through cryopolymerization with subsequent freeze drying. The obtained CBA was immersed in $CuSO_4$ solution to adsorb and anchor $Cu^{2+}$ onto the aerogel surface through electrostatic interaction and chelation. Dilute hydrazine hydrate was subsequently added into this CBA-$Cu^{2+}$ dispersion, followed by mixing at room temperature. Oxidation–reduction reaction occurred in the CBA-$Cu^{2+}$ precursor solution, inducing formation of the desired $Cu_2O$ NP-decorated CBA. In this way, ultrafine $Cu_2O$ NPs were well dispersed on the surface and inner wall of the CBA.

In this process, the effects of reaction time and $CuSO_4$ solution concentration on the structure, morphology, and photocatalytic activity of the $Cu_2O$/CBA composite catalysts were investigated to determine the optimal conditions. Figure 1 clearly shows the evolution of the crystal structure of the prepared $Cu_2O$/CBA composite catalysts when changing the reduction time. For reduction time of 5 or 10 min, the diffraction peaks observed at $2\theta = 29.36°$, 36.45°, 42.38°, 61.57°, 73.69°, and 77.65° correspond to 110, 111, 200, 220, 311, and 222 crystal planes of crystalline $Cu_2O$, respectively. However, characteristic peaks of the $Cu(OH)_2$ precursor were also detected at $2\theta = 32.55°$, 37.99°, 54.97°, and 65.53°. These diffraction peaks of the $Cu(OH)_2$ precursor disappeared for reduction time of 20 min, and all the diffraction peaks could be indexed to octahedral phase $Cu_2O$. When the reduction time was extended to 60 min, the intensity of the characteristic peak of $Cu_2O$ at 42° decreased, whereas that of Cu at 43° increased rapidly. This result indicates that some of the $Cu_2O$ gradually converted to Cu particles with increasing reduction time. Such a phenomenon was also reported by Tu et al. To determine the optimal reduction time, we further investigated the photocatalytic activity of the $Cu_2O$/CBA composite catalysts obtained using different reduction times, as shown in Fig. S1a. Compared with control, all the $Cu_2O$/CBA composite catalysts exhibited considerable photodegradation efficiency of MB dye. Notably, sample CCs-20 (obtained with reduction time of 20 min) showed the best photodegradation properties. Correspondingly, the highest content of $Cu_2O$ was achieved after 20 min of reduction according to AAS analysis (Table 1). Therefore, the samples mentioned hereinafter were fabricated using 20 min reaction time.

$Cu_2O$/CBA composite catalysts reduced with different $CuSO_4$ concentrations were then prepared. Figure 2 shows the interconnected 3D porous structure of the $Cu_2O$/CBA composite catalysts, with regular octahedral $Cu_2O$ NPs anchored onto the CBA surface, including the inner surface of the entire wall. With increasing $CuSO_4$ concentration, the average diameter of the $Cu_2O$ NPs decreased to 70.69 nm (CCs100) according to the distribution histograms in Fig. 2m–p. Compared with other samples, CCs100 showed the smallest size of $Cu_2O$ NPs, mainly ranging from 20 to 140 nm. EDS analysis also revealed the presence of Cu in the CCs100 composite catalyst (Fig. 3a). With increasing $CuSO_4$ concentration, more $Cu_2O$ NPs appeared on the aerogel surface, as verified by the increasing $Cu_2O$ content according to AAS analysis (Table 1). Furthermore, the photodegradation rate of the $Cu_2O$/CBA composite catalysts obtained using different $CuSO_4$ concentrations was also investigated and is shown in Fig. S1b. All samples exhibited excellent photocatalytic activity for degradation of MB, reaching approximately 90% within 240 min

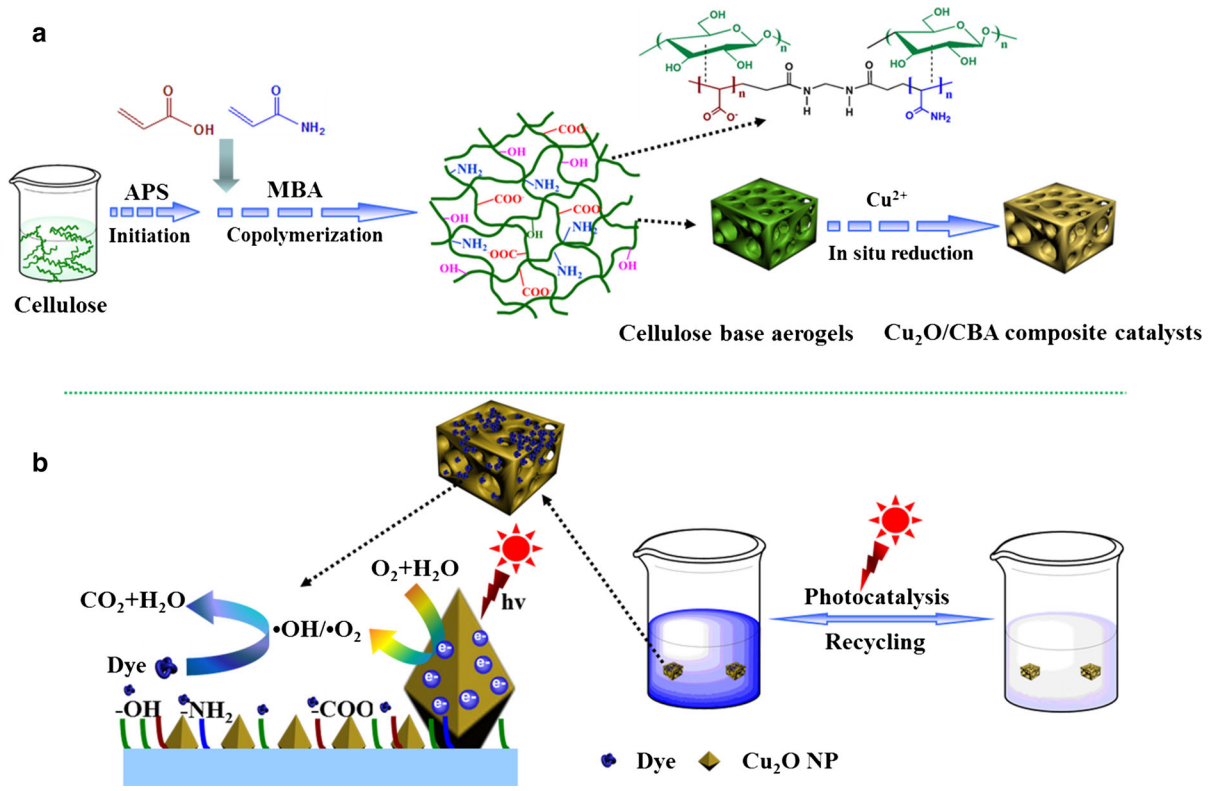


**Scheme 1** **a** Schematic for synthesis of $Cu_2O$/CBA composite catalysts. **b** Photocatalytic degradation of dye on surface of $Cu_2O$/CBA composite catalysts under visible-light irradiation

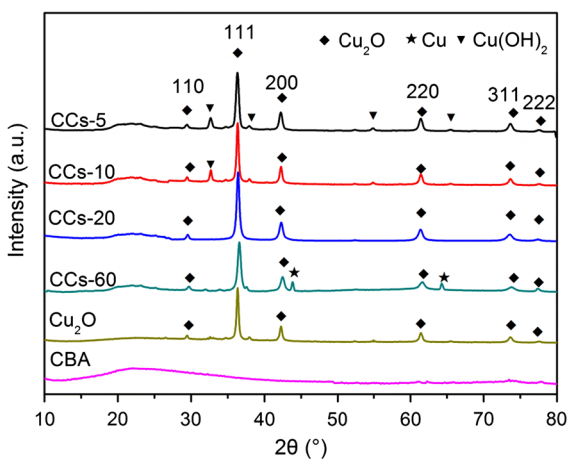


**Fig. 1** XRD patterns of $Cu_2O$/CBA composite catalysts obtained with different reduction times

under visible light. The highest photodegradation rate of more than 95.08% in 240 min was observed for sample CCs100. Meanwhile, the photodegradation rates for CCs12.5, CCs25, and CCs50 were 87.12, 91.05, and 92.32%, respectively. These results can be attributed to the higher $Cu_2O$ contents of the $Cu_2O$/CBA composite catalysts with stronger degradation properties according to AAS analysis.

**Table 1** $Cu_2O$ content and MB photodegradation rate after 240 min of irradiation for $Cu_2O$/CBA composite catalysts

| Sample | $Cu_2O$/gel (mg $g^{-1}$) | Degradation rate (%) |
|---|---|---|
| CCs-5 | 5.47 | 49.94 |
| CCs-10 | 8.64 | 56.97 |
| CCs-20 | 15.42 | 64.72 |
| CCs-60 | 15.23 | 77.25 |
| CCs12.5 | 19.70 | 87.12 |
| CCs25 | 32.10 | 91.05 |
| CCs50 | 46.00 | 92.32 |
| CCs100 | 50.00 | 95.08 |

Based on the results presented above, sample CCs100 prepared using 100 mmol $L^{-1}$ $CuSO_4$ solution and reduction time of 20 min was chosen for further investigation of representative material performance. The results in Fig. 3b reveal the chemical

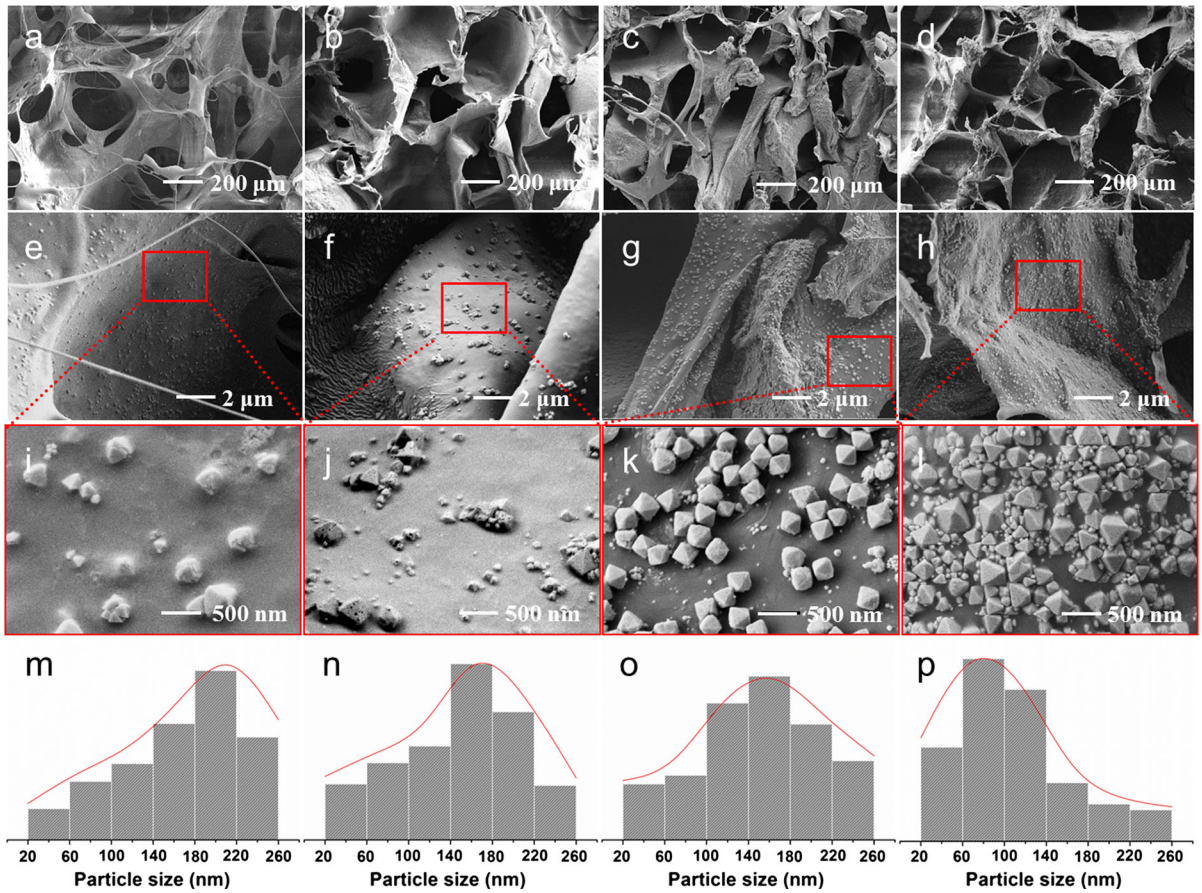


**Fig. 2** FESEM images of **a**, **e**, **i** CCs12.5, **b**, **f**, **j** CCs25, **c**, **g**, **k** CCs50, and **d**, **h**, **l** CCs100 composite catalysts at different magnifications, and particle size distributions of $Cu_2O$ NPs in **m** CCs12.5, **n** CCs25, **o** CCs50, and **p** CCs100

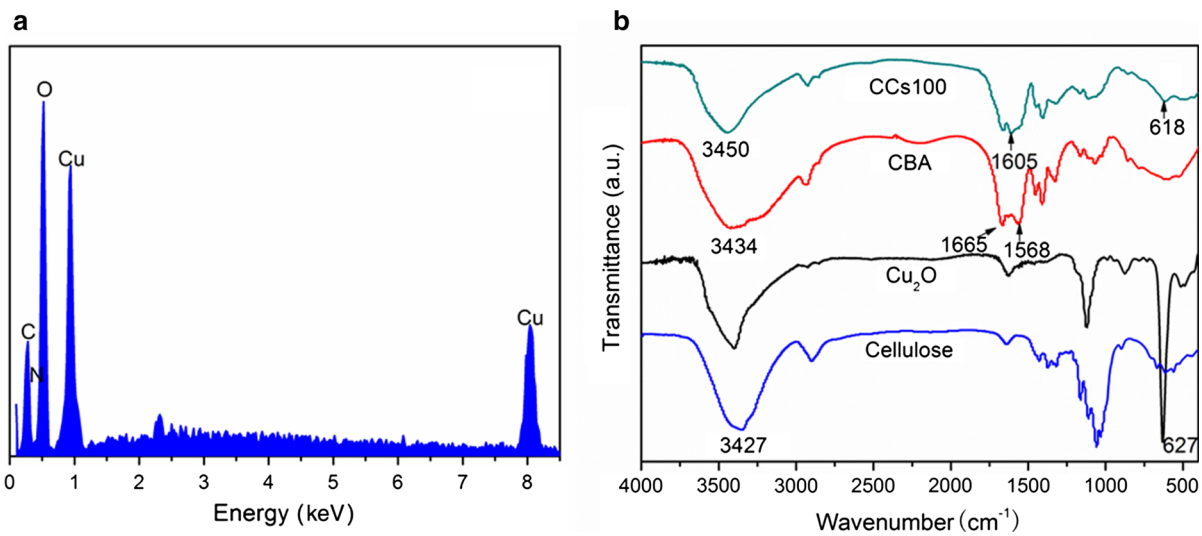


**Fig. 3** **a** Typical EDS pattern of CCs100, and **b** FTIR spectra of cellulose, pure $Cu_2O$, CBA, and CCs100

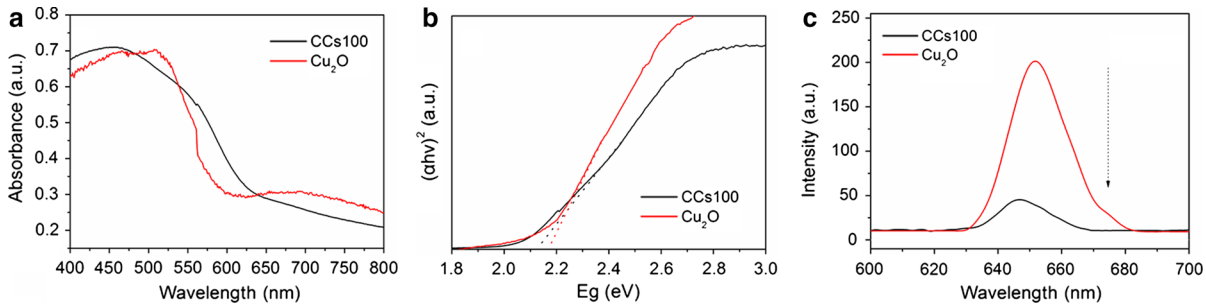


**Fig. 4** **a** UV–Vis absorption spectra of CCs100 and pure $Cu_2O$, **b** bandgap evaluation from plots of $(ahv)^2$ versus $hv$, and **c** PL spectra of CCs100 and pure $Cu_2O$

structure of cellulose, pure $Cu_2O$, CBA, and CCs100. In the spectrum for cellulose, the characteristic peaks at 3427, 2912, 1440, 1378, 1123, 1067, and 895 $cm^{-1}$ are typical bands of cellulose molecules (Liu et al. 2015). For pure $Cu_2O$, the peak at 627 $cm^{-1}$ was assigned to the characteristic peak of cuprous oxide (Yang et al. 2006). Compared with the spectrum for cellulose, CBA showed new peaks at 1665 and 1568 $cm^{-1}$, which were attributed to stretching vibration of CO–NH and asymmetric stretching vibration of COOH, respectively. The peak at 3434 $cm^{-1}$ became wider as a result of N–H stretching vibration, overlapping with O–H group signal. These results indicate that acrylic acid and acrylamide monomers were successfully grafted onto cellulose molecules. After in situ deposition of $Cu_2O$, the 3434 $cm^{-1}$ peak of N–H and O–H stretching vibration in the spectrum for CBA shifted to 3450 $cm^{-1}$, indicating attraction among –NH, –OH, and $Cu_2O$ NPs. Moreover, a shift of the $–COO^-$ stretching vibration signal from 1568 to 1605 $cm^{-1}$ was observed because of the attraction between $–COO^-$ and $Cu_2O$. The shift from 627 to 618 $cm^{-1}$ of the characteristic peak of $Cu_2O$ indicates interaction between CBA and cuprous oxide in sample CCs100 (Prabhakaran and Murugan 2014; Xu et al. 2007). These findings indicate strong interaction between the CBA and cuprous oxide NPs through hydroxy, amino, and carboxyl groups of the aerogel (Zeng et al. 2010). TG analysis also verified the presence of strong interaction between CBA and $Cu_2O$ NPs; i.e., the weight loss rate of sample CCs100 was less than 5 wt% before and after ultrasonic treatment at 350 W for 10 min (Fig. S2).

The optical properties of the samples were investigated by UV–Vis absorbance spectroscopy and PL spectroscopy. The UV–Vis absorption spectra of the representative CCs100 sample and pure $Cu_2O$ are presented in Fig. 4a. Pure $Cu_2O$ exhibited strong absorption in the visible-light region from 400 to 600 nm. After deposition of $Cu_2O$ onto CBA, the absorption region (400–650 nm) widened significantly, indicating good visible-light response for sample CCs100. This result can be attributed to the good macroporous structure and enlarged surface area, which enhance the efficiency of light harvesting (Wei et al. 2015). The energy bandgap of the two products was calculated using $(\alpha hv)^2 = A(hv - E_g)$, where $A$, $\alpha$, and $hv$ are the light absorption value, absorption coefficient, and discrete photon energy, respectively (Yi et al. 2010). Plots of $(\alpha hv)^2$ versus the photon energy ($hv$) of the absorbed light are displayed in Fig. 4b. From the intercepts of the tangents to the ($hv$) versus photon energy ($hv$) plots, the $E_g$ value (2.13 eV) of sample CCs100 was slightly lower than that (2.17 eV) for pure $Cu_2O$, indicating that introduction of CBA could narrow the energy gap of $Cu_2O$ to some extent. These results reveal that $Cu_2O$/CBA composites may be promising photocatalysts for photodegradation of contaminants under visible-light irradiation. Furthermore, the photoluminescence (PL) spectra was utilized to analyze the separation of photogenerated electrons and holes (Qamar et al. 2015). Figure 4c shows the PL spectra for CCs100 and pure $Cu_2O$. PL emission originates from recombination of photogenerated electron–hole pairs, thus the decreased PL intensity for CCs100 reveals high separation efficiency of photogenerated electron–hole pairs. These results suggest that in situ deposition of $Cu_2O$ on a cellulose matrix promoted light utilization and charge transfer, consequently enhancing the photocatalytic performance.

## Photocatalytic activity

The photocatalytic performance of the $Cu_2O$/CBA composite catalysts was investigated using CCs100 as representative catalyst and MB as model pollutant. In degradation tests, the CCs100 dose, initial MB concentration, and solution pH were optimized to achieve maximum photodegradation efficiency. Furthermore, the photocatalytic kinetics were determined using the Langmuir–Hinshelwood pseudo-first-order kinetic model (PFOKM) (McMurray et al. 2004). The pseudo-first-order equation was expressed in linear form as

$$\ln \frac{c_t}{c_0} = -k, \tag{2}$$

where $c_0$ (mg $L^{-1}$) is the dye concentration at zero irradiation time, $c_t$ is the dye concentration at irradiation time $t$ (min), and $k$ ($min^{-1}$) is the corresponding rate constant.

## Effects of dose on photocatalytic activity

The catalyst dose plays a crucial role in the photodegradation efficiency. Different CCs100 doses in the range of 0.3–1.0 g $L^{-1}$ were dispersed into 50 mL solution of MB at concentration of 20 mg $L^{-1}$. Before light irradiation, adsorption equilibrium was achieved by agitation at 120 rpm for 120 min in the dark. Figure 5 shows the relationship between the photodegradation rate and irradiation time for different CCs100 doses, as well as the PFOKM fits (shown in inset). As expected, the photodegradation efficiency increased with the catalyst dose, as a result of more binding sites being available for degradation. In addition, the data in Fig. 5 clearly show that the degradation rate increased sharply within the initial 30 min, then rose slowly. The corresponding rate constants ($k$) for CCs100, as calculated from the slopes of these plots, were 0.45, 0.56, 0.60, and 0.98 $min^{-1}$ (shown in inset). The reactivity of CCs100 at 1.0 g $L^{-1}$ was two times higher than at 0.3 g $L^{-1}$, verifying the enhanced photodegradation efficiency at higher catalyst dose. However, the concentration of 0.8 g $L^{-1}$ showed equally good degradation performance as 1.0 g $L^{-1}$ and was therefore chosen as the standard for subsequent experiments.

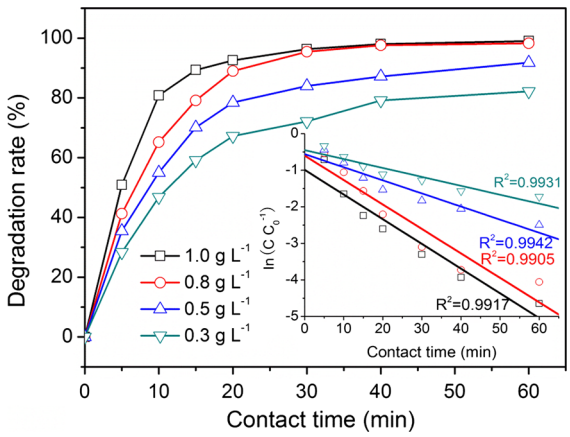


**Fig. 5** Effect of catalyst dose on photodegradation rate (pH 5.8, $c_0 = 20$ mg $L^{-1}$). *Inset* plot of $\ln(c/c_0)$ versus irradiation time

## Effect of initial MB concentration on photocatalytic activity

The effect of the initial MB concentration on the photocatalytic activity was also studied by immersing CCs100 (0.8 g $L^{-1}$) into 50 mL MB solution in the range of 25–100 mg $L^{-1}$. Figure 6 shows that, after 60 min of irradiation, the degradation rate of MB reached 98.23, 98.27, 90.56, and 84.79% at MB concentration of 25, 50, 75, and 100 mg $L^{-1}$, respectively. Meanwhile, the corresponding $k$ values for the MB degradation reaction were 0.57, 0.61, 0.34, and 0.26 $min^{-1}$, respectively (shown in inset). This trend is due to the limited number of reactive sites on the surface of a given quantity of CCs100, consistent with the results reported by Cao et al. (2013).

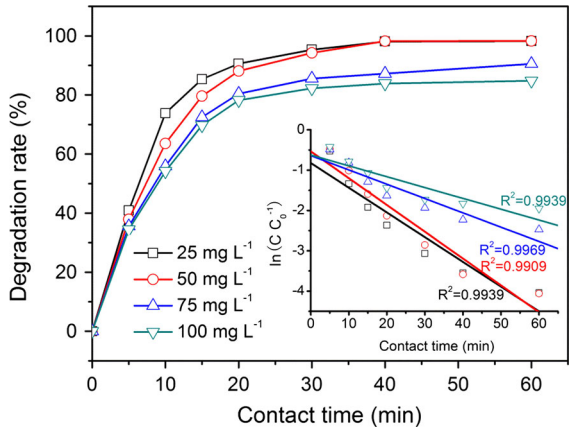


**Fig. 6** Effect of initial MB concentration on photodegradation rate [pH 5.8, (Cata.) = 0.8 g $L^{-1}$]. *Inset* plot of $\ln(c/c_0)$ versus irradiation time

## Effect of pH on photocatalytic activity

To evaluate the effect of pH on the photodegradation of MB, we dispersed 0.8 g $L^{-1}$ CCs100 into 50 mL of 20 mg $L^{-1}$ MB solution. The pH of the solution was adjusted to 3.0, 5.8, 7.0, and 9.0 using HCl and NaOH. The results in Fig. 7 show that higher degradation rate was achieved in acidic solution. After 60 min of irradiation, the degradation rate reached 98.56 and 97.27% at pH 3.0 and 5.8, but 79.09 and 56.2% at pH 7.0 and 9.0, respectively. The $k$ values for the dye degradation reaction were 0.59, 0.54, 0.19, and 0.10 $min^{-1}$ at pH 3.0, 5.8, 7.0, and 9.0, respectively. These results confirm that the photodegradation of MB was more efficient in acidic solution. In acidic medium, MB molecules (with two dimethylamino groups) are protonated and easily adsorb onto CCs100 (with negative surface charge). Consequently, MB was degraded more directly by hydroxyl radicals generated under visible-light irradiation. Such observations were also reported in previous studies (Cao et al. 2013; Habibi et al. 2005; Carrier et al. 2009).

## Recycling performance

A practical photocatalyst should be stable enough for repeated application. To evaluate the stability of the photodegradation performance of the CCs100 composite catalyst, we performed cycling tests of MB photodegradation by simply washing with distilled water for the next reaction cycle. CCs100 exhibited good stability after four reaction cycles, showing more than 90% degradation rate within 30 min. After six cycles, the degradation rate still remained at 80% within 30 min (Fig. 8), indicating good durability. This degradation performance is considerably better than that reported previously for pure unsupported $Cu_2O$ (Zheng et al. 2009), indicating that use of CBA evidently improved the stability of $Cu_2O$ during photodegradation. The electronic properties of the surface species, as determined by XPS analysis, also confirmed the good catalytic stability of $Cu_2O$. The XPS spectra of $Cu_{2p}$ in CCs100 before and after the sixth reaction cycle are shown in Fig. S3. Main binding energies of Cu $2p_{1/2}$ at 951.38 eV and Cu $2p_{3/2}$ at 931.68 eV were observed, being attributed to $Cu^+$ species in CCs100 (Zhang et al. 2014a). After the sixth reaction cycle, these peaks at 951.38 and 931.68 eV showed no change, indicating retention of the $Cu^+$ species. Thereby, one can consider that $Cu_2O$ NPs anchored on CBA are sufficiently stable during the photocatalytic process.

## Photocatalytic mechanism

The adsorption and photocatalytic activity of $Cu_2O$ octahedra, $Cu_2O$-b-CBA, and CCs100 for degradation of MB were also investigated using different time intervals and atmospheres, to understand the photocatalytic mechanism of the $Cu_2O$/CBA composite catalysts. The adsorption rate of MB onto the three samples increased sharply within 60 min, then rose slowly, and reached equilibrium in 120 min (Fig. 9a). The $Cu_2O$-b-CBA and CCs100 composite catalysts

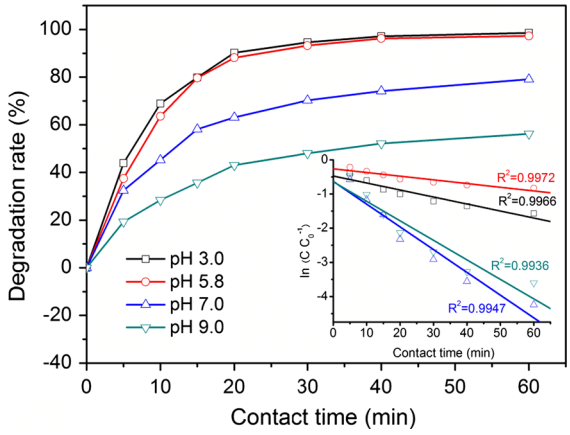


**Fig. 7** Effect of initial pH on photodegradation rate [$c_0$ = 20 mg $L^{-1}$, (Cata.) = 0.8 g $L^{-1}$]. *Inset*: plot of ln($c/c_0$) versus irradiation time

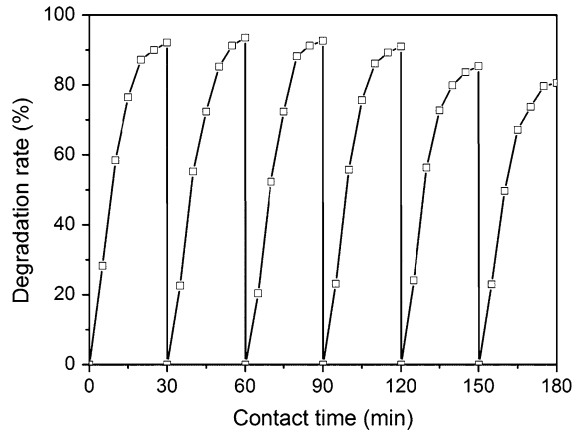


**Fig. 8** Stability study of CCs100 for photodegradation of MB under visible-light irradiation in six consecutive test cycles

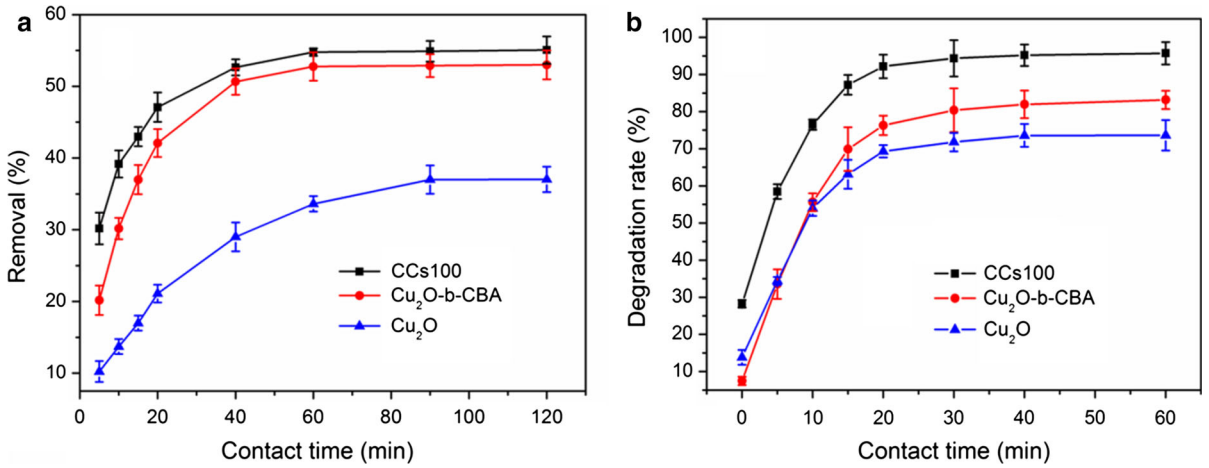


**Fig. 9** **a** Removal and **b** photodegradation rates of pure $Cu_2O$, $Cu_2O$-b-CBA, and CCs100 for MB dye

exhibited higher adsorption rates for MB (52.99 and 55.06%) compared with $Cu_2O$ (37.01%), but the adsorption ability of $Cu_2O$-b-CBA and CCs100 was almost the same. The relatively higher adsorption rates of MB onto $Cu_2O$-b-CBA and CCs100 can be explained by the abundant functional groups and pore structure of CBA. After light irradiation, photocatalytic reaction occurred, and the data indicated increased photocatalytic activity with increasing irradiation time (Fig. 9b). The degradation ability of $Cu_2O$ octahedra was about 73.59% within 60 min. After incorporation of CBA, both $Cu_2O$-b-CBA and CCs100 showed enhanced photodegradation of MB of 83.19 and 95.79%. The remaining concentration of MB after treatment with $Cu_2O$-b-CBA was approximately 17%, whereas for CCs100 it was approximately 4%. This high photocatalytic activity of CCs100 is due to not only its high adsorption ability for MB, but also the remarkable synergistic effect of the molecule interfacial layers (Chen et al. 2008).

$O_2$ or $N_2$ was also bubbled into 50 mL MB solution (20 mg $L^{-1}$) during the photocatalytic reaction with 0.8 g $L^{-1}$ CCs100 at pH 5.8. As shown in Fig. 10, the degradation rate of MB in oxygen atmosphere reached 99.01%, but only 53.21% under nitrogen atmosphere, after 60 min of visible-light irradiation. The $k$ values for the MB degradation reaction were 0.69 and 0.20 $min^{-1}$ (shown in inset) in the presence of oxygen and nitrogen atmosphere, respectively. The $k$ value under the oxygen atmosphere is more than three times higher than that under nitrogen. The higher rate constant obtained in the $O_2$ atmosphere can be explained by the fact that electrons produced by excited cuprous oxide can be captured by $O_2$ to yield $O_2^-$. Then, $O_2^-$ reacted with $H_2O$ molecule and electrons to produce $^{\cdot}OH$ and $H_2O_2$, which could effectively catalytically degrade dye molecules adsorbed on CCs100 (Zheng et al. 2009).

XPS was further used to probe the surface oxidation states of $Cu_2O$-b-CBA and CCs100. As shown in Fig. 11b, the O 1*s* signal for $Cu_2O$-b-CBA could be decomposed into two peaks with binding energy of 531.0 and 531.8 eV, assigned to O in CBA and adsorbed $O_2$, respectively. A peak assignable to O in $Cu_2O$ was not observed because of the low intensity of this signal. For CCs100, the O 1*s* signal could be

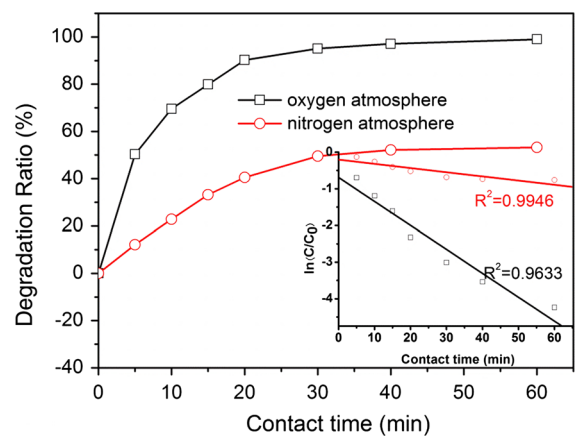


**Fig. 10** Effect of oxygen and nitrogen atmosphere on photocatalytic degradation of MB [$c_0$ = 20 mg $L^{-1}$, (Cata.) = 0.8 g $L^{-1}$, pH 5.8]. *Inset* plot of $\ln(c/c_0)$ versus irradiation time

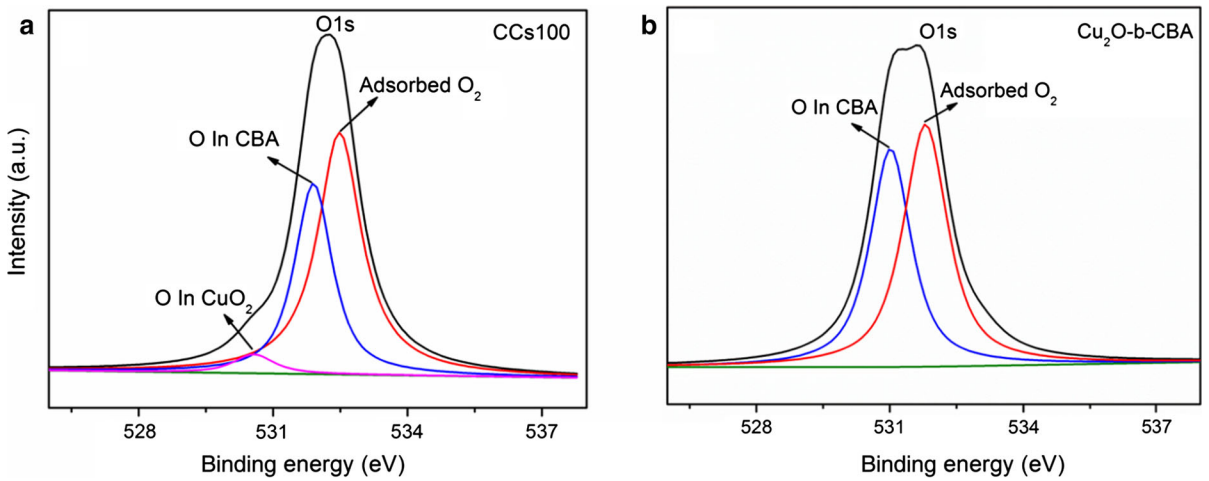


**Fig. 11** XPS spectra of O 1*s* peaks for **a** CCs100 and **b** $Cu_2O$-b-CBA

decomposed into three peaks (Fig. 11a). The peaks at 531.4 and 531.8 eV were assigned to O in CBA and adsorbed $O_2$, while the small peak at 529.2 eV was attributed to O in $Cu_2O$ (Zhang et al. 2007). Moreover, the area fraction of the peak for adsorbed $O_2$ was higher for CCs100 (60%) than $Cu_2O$-b-CBA (53%), confirming the stronger adsorption ability of CCs100. Consequently, the specific surface area of CCs100 (89.56 $m^2\ g^{-1}$, Fig. S4a) was much higher than that of $Cu_2O$-b-CBA (68.27 $m^2\ g^{-1}$, Fig. S4b). Thus, the enhanced photocatalytic activity of the $Cu_2O$/CBA composite catalysts can be attributed to their high specific surface area and oxygen adsorption capacity.

Furthermore, a free-radical trapping experiment was performed to investigate the main active radicals by adding various scavengers to the MB aqueous solution during the photochemical process. In this work, 0.5 mM *p*-benzoquinone (BQ) was used to quench $^{\cdot}O_2$ radical, isopropyl (IPA) for $^{\cdot}OH$ radical, and potassium iodide (KI) for $h^+$. As shown in Fig. 12, the photocatalytic efficiency of CCs100 was slightly affected by addition of KI. However, the photocatalytic activity of CCs100 was significantly inhibited when BQ or IPA was added to the photocatalytic reaction system (Liu et al. 2014). Therefore, $^{\cdot}O_2$ and $^{\cdot}OH$ should be the two main active species during photocatalytic degradation of MB by the $Cu_2O$/CBA composite catalysts under visible-light irradiation.

Because heterogeneous photocatalysis mainly occurs in molecule interfacial layers, the three main approaches to enhance the performance of a photocatalyst are to increase the adsorption of pollutants, extend the light absorption, and trap and shut photogenerated electrons (Chen et al. 2008). Based on results of FESEM and Brunauer–Emmett–Teller (BET) analyses, the $Cu_2O$/CBA composite catalysts with ample active sites exhibited rough and porous surfaces, increasing their specific surface area to enhance adsorption. Meanwhile, XPS and PL analyses showed that in situ $Cu_2O$ deposition on CBA could improve the surface chemisorbed oxygen species and photogenerated carrier separation efficiency, in turn facilitating electron capture and yielding more reactive oxidative species ($^{\cdot}O_2$/$^{\cdot}OH$) under light irradiation. Consequently, recombination of photogenerated electrons and holes was restrained, improving the photocatalytic activity of the $Cu_2O$/CBA composite catalysts. In addition,

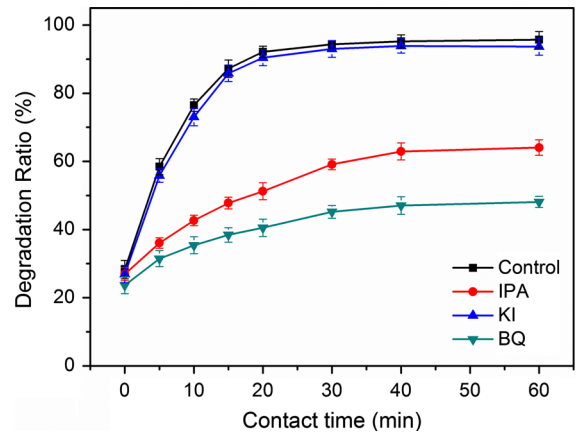


**Fig. 12** Photocatalytic activity of CCs100 in reactive species trapping experiments with three kinds of scavenger (IPA, KI, BQ)

introduction of CBA into the composite catalysts effectively extended the spectral response to visible light. In conclusion, the enhanced photocatalytic activity of the $Cu_2O$/CBA composite catalysts obtained by in situ deposition of $Cu_2O$ can be attributed to their unique structure with various favorable properties, viz. increased adsorption capability, separation of photogenerated charge carriers, and extended light absorption. A schematic illustrating the enhanced photocatalytic activity of the $Cu_2O$/CBA composite catalysts for degradation of MB is shown in Scheme 1b.

## Conclusions

$Cu_2O$ NP-functionalized CBA with 3D macroporous structure and abundant active sites was successfully prepared for visible-light-responsive photocatalysis via in situ deposition of $Cu_2O$ NPs on CBA. Octahedral $Cu_2O$ NPs were formed and anchored onto the surface and inner wall of the cellulose matrix, preventing aggregation and protecting the catalytic character of the NPs. The photocatalytic activity of the $Cu_2O$/CBA composite catalysts was evidently enhanced compared with pure $Cu_2O$ octahedra or $Cu_2O$-b-CBA. Such enhanced photocatalytic activity of the $Cu_2O$/CBA composite catalysts obtained through in situ deposition of $Cu_2O$ can be attributed to a combination of increased adsorption capacity due to their 3D porous structure and abundant active sites, separation of photogenerated electrons and holes via adsorbed molecular oxygen, as well as extended light absorption via introduction of the cellulose matrix. The presented results indicate that these $Cu_2O$/CBA composites are excellent, recyclable, visible-light-driven photocatalysts, having potential applications in pollutant degradation and water treatment.

**Acknowledgments** The work is financially supported by the National Science Foundation of China (51303159, 51372226), National Science Foundation of Zhejiang Province (LQ13E030008, LY15E030003), and Program for Zhejiang Top Priority Discipline of Textile Science and Engineering (2013YXQN06).

## References

Arcot LR, Uddin KMA, Chen X, Xiang WC, Kong XM, Johansson LS, Ras RHA, Rojas OJ (2015) Paper-based plasmon-enhanced protein sensing by controlled nucleation of silver nanoparticles on cellulose. Cellulose 22(6):4027–4034

Cao CH, Xiao L, Liu L, Zhu HY, Chen CH, Gao L (2013) Visible-light photocatalytic decolorization of reactive brilliant red x-3b on $Cu_2O$/crosslinked-chitosan nanocomposites prepared via one step process. Appl Surf Sci 271:105–112

Cao H, Yang A, Li H, Wang L, Li S, Kong J, Yang R (2015) A non-enzymatic glucose sensing based on hollow cuprous oxide nanospheres in a Nafion matrix. Sensor Actuators B Chem 214:169–173

Carrier M, Guillard C, Besson M, Bordes C, Chermette H (2009) Photocatalytic degradation of diuron: experimental analyses and simulation of HO radical attacks by density functional theory calculations. J Phys Chem A 113:6365–6374

Chen JY, Zhou PJ, Li JL, Wang Y (2008) Studies on the photocatalytic performance of cuprous oxide/chitosan nanocomposites activated by visible light. Carbohydr Polym 72:128–132

Chiappone A, Nair JR, Gerbaldi C, Bongiovanni R, Zeno E (2013) Nanoscale microfibrillated cellulose reinforced truly-solid polymer electrolytes for flexible, safe and sustainable lithium-based batteries. Cellulose 20(5):2439–2449

Habibi MH, Hassanzadeh A, Mahdavi S (2005) The effect of operational parameters on the photocatalytic degradation of three textile azo dyes in aqueous $TiO_2$ suspensions. J Photochem Photobiol A 172:89–96

Han WJ, Ren L, Gong LJ, Qi X, Liu YD, Yang LW, Wei XL, Zhong JX (2014) Self-assembled three-dimensional graphene-based aerogel with embedded multifarious functional nanoparticles and its excellent photoelectrochemical activities. ACS Sustain Chem Eng 2(4):741–748

Han YY, Wu XD, Zhang XX, Zhou ZH, Lu CH (2016) Reductant-free synthesis of silver nanoparticles-doped cellulose microgels for catalyzing and product separation. ACS Sustain Chem Eng. doi:10.1021/acssuschemeng.6b00889

Hua Q, Shang DL, Zhang WH, Chen K, Chang SJ, Ma YS, Jiang ZQ, Yang JL, Huang WX (2011) Morphological evolution of $Cu_2O$ nanocrystals in an acid solution: stability of different crystal planes. Langmuir 27:665–671

Huang WC, Lyu LM, Yang YC, Huang MH (2012) Synthesis of $Cu_2O$ nanocrystals from cubic to rhombic dodecahedral structures and their comparative photocatalytic activity. J Am Chem Soc 134:1261–1267

Li Q, Cao RG, Cho J, Wu G (2014) Nanocarbon electrocatalysts for oxygen reduction in alkaline media for advanced energy conversion and storage. Adv Energy Mater 4(6):737–740

Liu J, Yang YM, Liu NY, Liu Y, Huang H, Kang ZH (2014) Total photocatalysis conversion from cyclohexane to cyclohexanone by $C_3N_4$/Au nanocomposites. Green Chem 16:4559–4565

Liu L, Gao ZY, Su XP, Chen X, Jiang L, Yao JM (2015) Adsorption removal of dyes from single and binary solutions using a cellulose-based bioadsorbent. ACS Sustain Chem Eng 3:432–442

Majhi SM, Rai P, Raj S, Chon BS, Park KK, Yu YT (2014) Effect of Au nanorods on potential barrier modulation in

morphologically controlled Au@$Cu_2O$ core–shell nanoreactors for gas sensor applications. ACS Appl Mater Interfaces 6:7491–7497

McMurray TA, Byrne JA, Dunlop PSM, Winkelman JGM, Eggins BR, McAdams ET (2004) Intrinsic kinetics of photocatalytic oxidation of formic and oxalic acid on immobilised $TiO_2$ films. Appl Catal A Gen 262:105–110

Prabhakaran G, Murugan R (2014) Synthesis of $Cu_2O$ nanospheres and cubes: their structural, optical and magnetic properties. Adv Mater Res 938:114–117

Qamar MT, Aslam M, Ismail IMI, Salah N, Hameed A (2015) Synthesis, characterization, and sunlight mediated photocatalytic activity of CuO coated ZnO for the removal of nitrophenols. ACS Appl Mater Interfaces 7:8757–8769

Sanad MMS, Shalan AE, Rashad MM, Mahmoud MHH (2015) Plasmonic enhancement of low cost mesoporous $Fe_2O_3$–$TiO_2$ loaded with palladium, platinum or silver for dye sensitized solar cells (DSSCs). Appl Surf Sci 359:315–322

Sun ZB, Li HZ, Cui GJ, Tian YX, Yan SQ (2016) Multifunctional magnetic core–shell dendritic mesoporous silica nanospheres decorated with tiny Ag nanoparticles as a highly active heterogeneous catalyst. Appl Surf Sci 360:252–262

Tilley SD, Schreier M, Azevedo J, Stefik M, Graetzel M (2014) Ruthenium oxide hydrogen evolution catalysis on composite cuprous oxide water-splitting photocathodes. Adv Funct Mater 24:303–311

Tu K, Wang QY, Lu A, Zhang LN (2014) Portable visible-light photocatalysts constructed from $Cu_2O$ nanoparticles and graphene oxide in cellulose matrix. J Phys Chem C 118:7202–7210

Wang XF, Chen GM, Zhang J (2013) RETRACTED: synthesis and characterization of novel $Cu_2O$/PANI composite photocatalysts with enhanced photocatalytic activity and stability. Catal Commun 31:57–61

Wei YC, Jiao JQ, Zhao Z, Zhong WJ, Li JM, Liu J, Jiang GY, Duan AJ (2015) 3D ordered macroporous $TiO_2$-supported Pt@CdS core–shell nanoparticles: design, synthesis and efficient photocatalytic conversion of $CO_2$ with water to methane. J Mater Chem A 3:11074–11085

Xiong R, Lu CH, Wang YR, Zhou ZH, Zhang XX (2013) Nanofibrillated cellulose as the support and reductant for the facile synthesis of $Fe_3O_4$/Ag nanocomposites with catalytic and antibacterial activity. J Mater Chem A 1:14910–14918

Xu YY, Chen DR, Jiao XL, Xue KY (2007) Nanosized $Cu_2O$/PEG400 composite hollow spheres with mesoporous shells. J Phys Chem C 111:16284–16289

Yang HM, Yang JO, Tang AD, Xiao Y, Li XW, Dong XD, Yu YM (2006) Electrochemical synthesis and photocatalytic property of cuprous oxide nanoparticles. Mater Res Bull 41:1310–1318

Yi ZG, Ye JH, Kikugawa N, Kako T, Ouyang SX, Stuart-Williams H, Yang H, Cao JY, Luo WJ, Li ZS, Liu Y, Withers RL (2010) An orthophosphate semiconductor with photooxidation properties under visible-light irradiation. Nat Mater 9:559–564

Zeng J, Liu SL, Cai J, Zhang LN (2010) $TiO_2$ immobilized in cellulose matrix for photocatalytic degradation of phenol under weak UV light irradiation. J Phys Chem C 114(17):7806–7811

Zhang YG, Ma LL, Li JL, Yu Y (2007) In situ Fenton reagent generated from $TiO_2$/$Cu_2O$ composite film: a new way to utilize $TiO_2$ under visible light irradiation. Environ Sci Technol 41(17):6264–6269

Zhang LZ, Jing DW, Guo LJ, Yao XD (2014a) In situ photochemical synthesis of Zn-doped $Cu_2O$ hollow microcubes for high efficient photocatalytic $H_2$ production. ACS Sustain Chem Eng 2(6):1446–1452

Zhang ZY, Sun T, Chen C, Xiao F, Gong Z, Wang S (2014b) Bifunctional nanocatalyst based on three-dimensional carbon nanotube-graphene hydrogel supported Pd nanoparticles: one-pot synthesis and its catalytic properties. ACS Appl Mater Interfaces 6(23):21035–21040

Zheng ZK, Huang BB, Wang ZY, Guo M, Qin XY, Zhang XY, Wang P, Dai Y (2009) Crystal faces of $Cu_2O$ and their stabilities in photocatalytic reactions. J Phys Chem C 113(32):14448–14453

Zhou ZH, Zhang XX, Lu CH, Lan LD, Yuan GP (2014) Polyaniline-decorated cellulose aerogel nanocomposite with strong interfacial adhesion and enhanced photocatalytic activity. RSC Adv 4(18):8966–8972